Journal of Hydrology 634 (2024) 131080

Contents lists available at ScienceDirect

Journal of Hydrology

journal homepage: www.elsevier.com/locate/jhydrol

Research papers

ENSO weakens the co-variability between the spring persistent rains and Asian summer monsoon: Evidences from tree-ring data in southeastern China

Feifei Zhou [a], Keyan Fang [a,*], Fredrik Charpentier Ljungqvist [b,c,d], Tinghai Ou [e], Jun Cheng [f], Fen Zhang [g], Zhengtang Guo [h,i]

[a] Key Laboratory of Humid Subtropical Eco-geographical Process (Ministry of Education), College of Geographical Sciences, Fujian Normal University, Fuzhou 350007, China
[b] Department of History, Stockholm University, SE-106 91 Stockholm, Sweden
[c] Bolin Centre for Climate Research, Stockholm University, SE-106 91 Stockholm, Sweden
[d] Swedish Collegium for Advanced Study, Linneanum, Thunbergsvägen 2, SE-752 38 Uppsala, Sweden
[e] Regional Climate Group, Department of Earth Sciences, University of Gothenburg, Box 460 SE-405 30, Gothenburg, Sweden
[f] Key Laboratory of Meteorological Disaster, Ministry of Education (KLME), Nanjing University of Information Science and Technology, Nanjing 210044, China
[g] Key Laboratory of Western China's Environmental Systems (MOE), Lanzhou University, Lanzhou 730000, China
[h] Excellence in Life and Paleoenvironment, Beijing 100044, China
[i] Institute of Geology and Geophysics, Chinese Academy of Sciences, Beijing 100029, China

ARTICLE INFO

This manuscript was handled by Huaming Guo, Editor-in-Chief

Keywords:
Tree rings
Earlywood and latewood
Oxygen isotope
El Niño–Southern Oscillation
Spring persistent rains
Asian summer monsoon

ABSTRACT

The Spring Persistent Rains (SPR) and the Asian Summer Monsoon (ASM) are the two dominant rainfall systems in East Asia, providing together a majority of annual rainfall in southeastern China (SEC). Since observational data in SEC were mostly unavailable until the 1950s, proxy records that are capable of capturing the SPR and ASM variations are required to examine the long-term co-variability patterns between them. Tree-ring earlywood and latewood $\delta^{18}O$ records in SEC were found to respond to relative humidity (RH) during the SPR and ASM seasons, respectively, allowing us, for the first time, to reconstruct the RH changes of SPR and ASM back to 1801. The two reconstructions can explain 44.9 % and 42.3 % of the instrumental variance. We observed a long-lasting wet epoch in the 1920s–60s for both the SPR and ASM, caused by a peak in the land–ocean thermal contrast. The El Niño-Southern Oscillation (ENSO) and the Intertropical Convergence Zone (ITCZ) were found to be the two leading tropical systems that modulated the SPR and ASM co-variability. During a period with weakened ENSO variance, the RH of SPR and ASM showed in-phase changes driven by the ITCZ. However, when the ENSO variance became strengthened, the co-variability collapsed since the ENSO can offset the influence of the ITCZ via teleconnections.

1. Introduction

The Asian Summer Monsoon (ASM) (from June to September) is the strongest regional monsoon system, providing the majority of summer rainfall in East Asia (Tao & Chen, 1987; Mao et al., 2004). However, eastern Asia is dominated by another critical rainy season, known as the Spring Persistent Rains (SPR), a unique climate phenomenon over eastern Asia (Tian & Yasunari, 1998; Wan & Wu, 2009). The SPR mainly occurs from March to May before the onset of the ASM due to the zonal land–sea thermal contrast and the mechanical forcing of the Tibetan Plateau, and the distribution of its rain belt is usually subject to the landforms of Wuyi Mountains (25–29° N, 116–119° E) and Nanling Mountains (24–26.5° N, 110–116° E) in southeastern China (SEC) (Wan & Wu, 2009). The ASM and SPR are two leading precipitation systems in eastern Asia, and they overlap with each other in SEC. Rainfall during the SPR and ASM accounts for about 75 % of the annual rainfall over SEC, and their contribution to the total rainfall is approximately equal (Yang & Lau, 2004). Due to a strong hydroclimate variability during the two seasons, floods or droughts regularly hit SEC, frequently having severe socio-economic impacts (Mao et al., 2004; Wu & Mao, 2016). A

* Corresponding author.
E-mail address: kfang@fjnu.edu.cn (K. Fang).

https://doi.org/10.1016/j.jhydrol.2024.131080
Received 1 February 2022; Received in revised form 2 March 2024; Accepted 4 March 2024
Available online 21 March 2024
0022-1694/

possible further increase in the frequency, duration, and severity of floods and droughts under projected global warming may pose threats for the stability of ecology and society alike (Piao et al., 2010; Amengual et al., 2014).

On the one hand, the hydroclimatic conditions during the SPR and ASM are modulated by the West Pacific Subtropical High (WPSH), the land–ocean thermal contrast, the thermal conditions of the Tibetan Plateau among other factors (Huang et al., 2004; Peng et al., 2005; Wan et al., 2008; Wan & Wu, 2009). Thus, hydroclimatic changes during the SPR and ASM seasons may be closely linked (Wan et al., 2008). On the other hand, the response patterns of the SPR and ASM with the El Niño–Southern Oscillation (ENSO) are distinct, i.e. a positive (negative) ENSO consistent with an increase (decrease) of the SPR (ASM) (Xu et al., 2013; Wu & Mao, 2016; Zhou et al., 2020). The correlations between the SPR and ASM seem to be weak during the instrumental period (**Fig. S1**). At present, considerable knowledge gaps remain with regard to the SPR and ASM co-variability, especially concerning the time-varying patterns of their co-variability. This is largely due to a lack of proxy data with seasonal resolution, covering long time periods, that can capture hydroclimate variations in the SPR and ASM seasons.

Tree-ring data (e.g. ring-width, stable isotopes) can capture exactly-dated, annually-resolved information about past hydroclimate (precipitation, drought, relative humidity, etc.) during the growth period or even during an entire hydrological year (Fang et al., 2015; Zhou et al., 2020; Ljungqvist et al., 2020). Tree rings are composed of earlywood and latewood, distinguished by the difference of the density owing to seasonal shifts (Fritts, 1976), and can potentially track different seasonal climatic changes (Griffin et al., 2013; Dannenberg & Wise, 2016; Tabari & Willems, 2018; Seftigen et al., 2020). Stable oxygen isotopes ($\delta^{18}O$) preserved in tree-ring cellulose are modulated by atmospheric vapor pressure deficit and source water isotope compositions during the formation of the cellulose (Loader et al., 1997; McCarroll & Loader, 2004; Bose et al., 2016; Managave et al., 2020). Tree-ring $\delta^{18}O$ records are a suitable archive for high-resolution hydroclimate reconstructions over the warm and humid SEC where tree-ring width data often has a weak hydroclimatic signal (Xu et al., 2013, 2016; Liu et al., 2017). As inferred from intra-annual observations (Zheng et al., 2022), the formation of earlywood of *Pinus massoniana* growing in SEC normally occurs in the SPR season, while latewood is produced in the ASM season. Thus, the tree-ring earlywood and latewood $\delta^{18}O$ signatures in SEC may

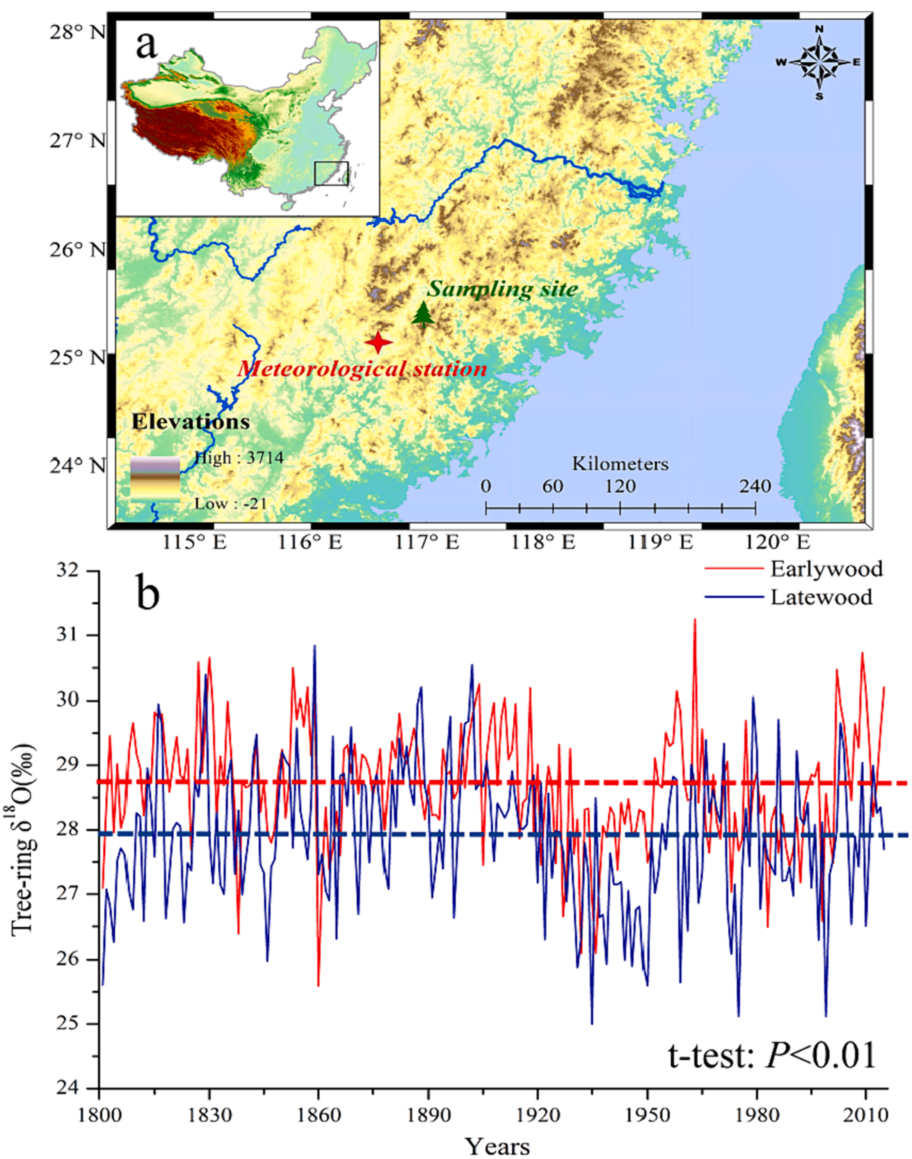

Fig. 1. A) map showing the locations of the tree-ring sampling site (tree) and the meteorological station (star) used in this study; b) the earlywood (red line) and latewood (blue line) $\delta^{18}O$ chronologies during the period 1801–2015. The dash lines symbolize the mean values of the two $\delta^{18}O$ records. (For interpretation of the references to colour in this figure legend, the reader is referred to the web version of this article.)

incorporate variations in local hydroclimate during the SPR and ASM, respectively.

In this study, earlywood and latewood $\delta^{18}O$ chronologies from *Pinus massoniana* trees in SEC are used to reconstruct hydroclimate changes during the SPR and ASM seasons, respectively, over the 1801–2015 period. The two reconstruction will provide a long-term context to assess the co-variability of the SPR and ASM variations, and investigate the atmospheric and oceanic circulation patterns modulating these variations.

2. Materials and methods

2.1. The $\delta^{18}O$ chronology development

The tree-ring $\delta^{18}O$ time-series employed in the present article are derived from cross-dated *Pinus massoniana* cores from the Makeng site (25.27°N, 117.35°E, 1000 m a.s.l) in SEC (Fig. 1**a**). These cores have been collected, cross-dated and measured for the development of a robust ring-width chronology by Wang et al. (2018). We herein selected six cores from six trees with no absent rings and homogeneous growth patterns for isotopic analysis, covering the 1801–2015 period. The boundary between the earlywood and latewood of *Pinus massoniana* is distinct (**Fig. S2**). They were carefully separated by a razor blade under a binocular microscope based on differences in their cell colors. We pooled the whole earlywood and latewood fractions of all the sampled trees for each year prior to α-cellulose extraction (Leavitt, 2010; Liu et al., 2009).

A modified version of the method mentioned by Green (1963) and Loader et al. (1997) was used for cellulose extraction. To homogenize the cellulose, the cellulose fibres were broken down with an ultrasound machine and then freeze-dried for 72 h with a vacuum freeze dryer prior to isotopic analysis. Approximately 0.15 mg of α-cellulose was packed in a silver capsule, and analyzed with an isotope ratio mass spectrometer interfaced with a pyrolysis-type high-temperature conversion elemental analyzer (TC/EA) to obtain cellulose. The $\delta^{18}O$ values were measured using a High Temperature Conversion Elemental Analyzer (TC/EA) coupled to a Finnigan MAT-253 mass spectrometer (Thermo Electron Corporation, Bremen, Germany) at the isotopic laboratory of Fujian Normal University, China. The Merck cellulose was used as the reference standard, which was inserted every eight samples during the measurements. Oxygen isotope results are presented in δ notation as the per mil (‰) deviation from Vienna Standard Mean Ocean Water (VSMOW):

$$\delta^{18}O = \left(\left(R_{sample}/R_{standard}\right) - 1\right)*1000$$

where R_{sample} and $R_{standard}$ are the $^{18}O/^{16}O$ ratios of the sample and standard, respectively. The analytical uncertainties for repeated measurements of the Merck cellulose were approximately ± 0.19 ‰.

2.2. Instrumental dataset

The meteorological station is located at Shanghang (25.05° N, 116.42° E, 198 m a.s.l), which is the closest one (~80 km) to the Makeng site (Fig. 1**a**). It is characterized by a humid and warm subtropical climate (**Fig. S3**). The instrumental monthly mean temperature, total precipitation and relative humidity (RH) records are used to investigate the relationships between tree-ring $\delta^{18}O$ and climate for the period from 1957 to 2015 (**Fig. S4**). Monthly sea surface temperatures (SSTs) and 850 hPa geopotential heights (GPHs) were employed to detect the impacts of oceanic-atmospheric circulation patterns on the co-variability of the hydroclimate in the SPR and ASM. The SSTs were derived from the HadISST1 dataset presented on a 0.5°×0.5° grid for the period from 1870 to 2015 (Rayner et al., 2003). The GPHs were obtained from the Twentieth Century Reanalysis (20CR) V3 (Compo et al., 2011; Slivinski et al., 2019), which provided a comprehensive global atmospheric circulation dataset spanning the 1836–2015 period with a resolution of 1°×1°. In addition, the observed and reconstructed ENSO variations (Wilson et al., 2010) were consulted to evaluate the modulations of ENSO on the co-variability between the SPR and ASM. The Niño 3.4 index (Trenberth & Stepaniak, 2001), the average SST anomalies from the HadISST1 dataset in the region bounded by 5° N to 5° S and 170° W to 120° W, were used herein to represent the observed ENSO.

2.3. Methods

The hydroclimate reconstruction was conducted through a simple linear regression model based on a split calibration and verification procedure designed to test the model reliability (Meko & Graybill, 1995). A number of statistic metrics were used to evaluate model ability, including simple Pearson's correlation coefficient (R), R square (R^2), reduction of error (RE) and coefficient of efficiency (CE). Values of RE and CE greater than zero normally indicate model skill. Moving correlations between the two reconstructions with a 50-yr sliding window are used to investigate the dynamics of the SPR and ASM co-variability through time. In additional, spatial correlation maps were produced by the KNMI Climate Explorer (Trouet & Van Oldenborgh, 2013) to identify the key oceanic and atmospheric modes.

3. Results

3.1. Earlywood and latewood $\delta^{18}O$ tree-ring series

We developed earlywood and latewood $\delta^{18}O$ chronologies of *Pinus massoniana* trees at the Makeng site during the 1801–2015 period (Fig. 1**b**). The earlywood $\delta^{18}O$ values ranged from 25.6 ‰ to 31.3 ‰ with an average of 28.7 ‰ (**Table S1**). The values for latewood $\delta^{18}O$ were lower, varying from 24.9 ‰ to 30.8 ‰, with a mean of 27.9 ‰. The annual standard deviations for the earlywood and latewood $\delta^{18}O$ were 0.9 ‰ and 1.1 ‰, respectively. A significant ($P < 0.01$) disparity was found between the earlywood and latewood time series by a student's *t*-test (Fig. 1**b**). The correlation between the two $\delta^{18}O$ time-series are significantly positive ($r = 0.41$, $p < 0.001$). The first-order autocorrelations for the earlywood and latewood $\delta^{18}O$ are 0.27 and 0.19, respectively, and the correlation of the latewood $\delta^{18}O$ in current years with the earlywood $\delta^{18}O$ in previous years is $r = 0.23$. The low correlation coefficients are indicative of a slight impact of physiological processes from prior years on the $\delta^{18}O$ values in current years.

3.2. Reconstructed relative humidity during the SPR and ASM

Correlation analysis was performed between the tree-ring $\delta^{18}O$ chronologies and monthly instrumental climate records (Fig. 2). As shown, both the earlywood and latewood $\delta^{18}O$ showed relatively weak associations with temperature and precipitation (Fig. 2**a, 2b**). Significant ($p < 0.01$) negative correlations were observed between the earlywood $\delta^{18}O$ and RH in the months of February, March, April and May, and the highest correlation with RH ($r = -0.67$, $P < 0.001$, $N = 59$) was observed when combining the months from March to May (Fig. 2**c**). For latewood $\delta^{18}O$, significant correlations with RH occurred from June to October. The highest correlation ($r = -0.65$, $P < 0.001$, $N = 59$) was found during the consecutive months from June to September. The response pattern between tree-ring $\delta^{18}O$ and RH variations in SEC was also reported by previous literature (Xu et al., 2013; Liu et al., 2017).

Spring (March–May) and summer (June–September) RH acted as the strongest predictants of variance in earlywood and latewood $\delta^{18}O$ in the study area and they were thus selected as the targets for the reconstruction. The linear regression models account for 44.9 % and 42.3 % of the actual variance of RH in the SPR and ASM, respectively (Fig. 3). As shown in **Table S2**, the values of RE and CE for the split sub-periods (i.e. 1957–1986 and 1987–2015) are positive, indicative of a sufficient model fit. Besides, the significant correlations between the interannual variability of observed and reconstructed RH also indicated the

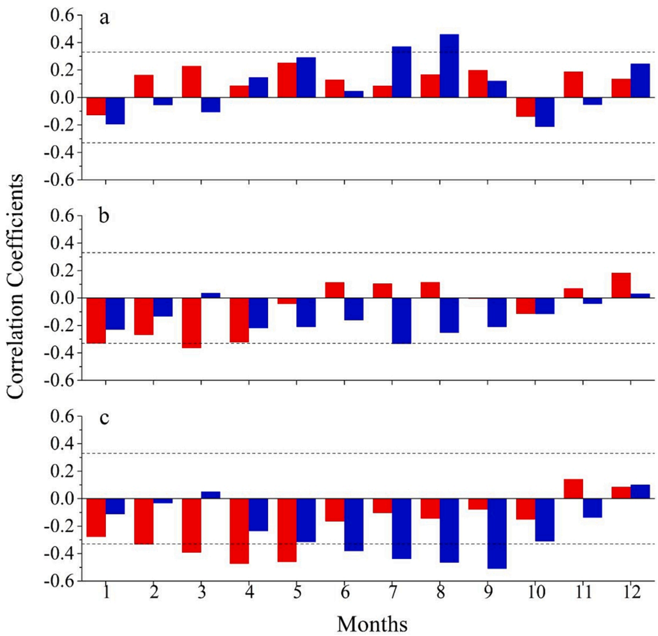

Fig. 2. The correlations of the earlywood (red bar) and latewood (blue bar) $\delta^{18}O$ with monthly temperature (a), precipitation (b) and relative humidity (c) over the common period of 1957–2015. (For interpretation of the references to colour in this figure legend, the reader is referred to the web version of this article.)

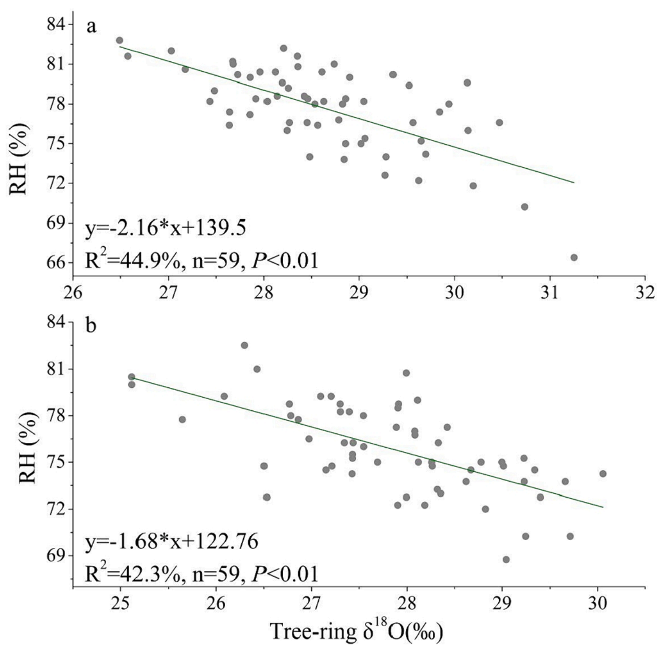

Fig. 3. The linear regression model of the earlywood (a) and latewood (b) $\delta^{18}O$ chronologies with the observed March–May (a) and June–September (b) RH.

robustness of our model (**Fig. S5**).Based on the two models, we reconstruct temporal changes of local RH of SPR and ASM since 1801 (Fig. 4**a, 4b**). To test the validity of the two reconstructions, we also correlated them with a tree-ring chronology known to be negatively associated with spring hydroclimate changes for the period 1801–2014 (Zhou et al., 2020) and a summer monsoonal rainfall reconstruction from tree-ring $\delta^{18}O$ for the period 1870–2014, nearby (Xu et al., 2013), respectively (**Fig. S6**). In addition, the spatial correlation patterns with gridded surface RH dataset revealed that the reconstructions can well indicate

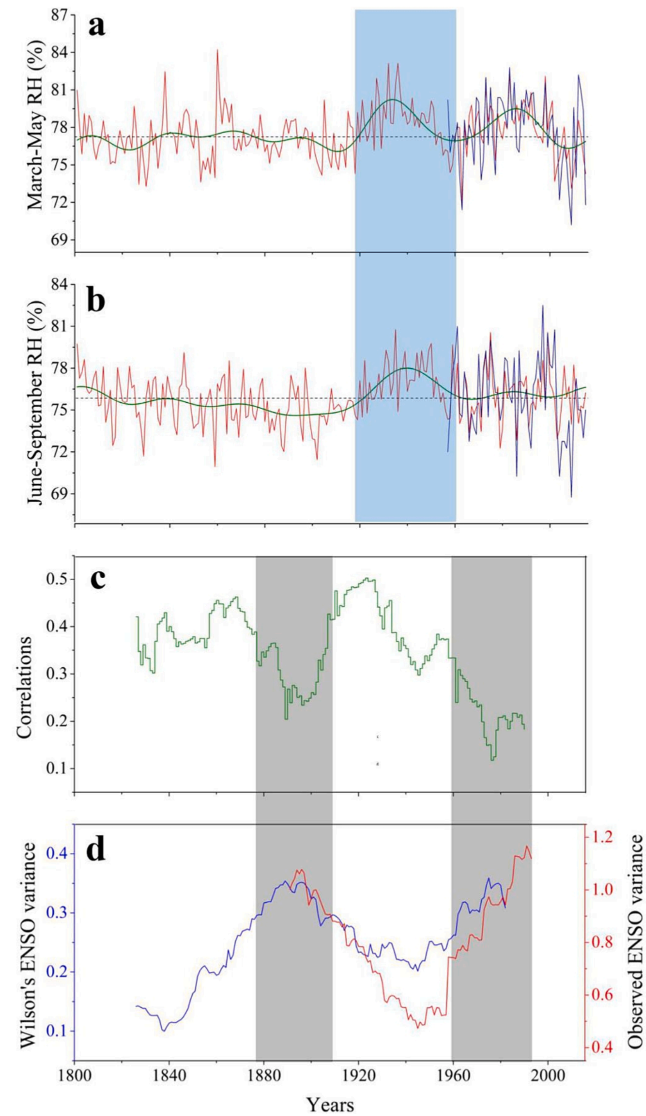

Fig. 4. The RH reconstructions (red line) back to 1801 during a) SPR and b) ASM, with the interdecadal variations (bold green line) isolated by using a 30-year fast-Fourier transform filter, the target time series (cyan line) for the 1951–2015 period of overlap and the long-term average value (dash line); c) The 31-year running correlations (assigned to center year of the window) between the SPR-ASM hydroclimate reconstructions; d) The 31-year running variance of the observed (red line) and reconstructed (blue line; Wilson et al., (2010)) ENSO indices (assigned to center year of the window). (For interpretation of the references to colour in this figure legend, the reader is referred to the web version of this article.)

large-scale hydroclimate changes in SPR and ASM (**Fig. S7**). These findings indicated that our reconstructions were capable of capturing hydroclimate features back across time and space for the SPR and ASM seasons across SEC.

3.3. The SPR and ASM co-variability

The sliding correlations between the two RH reconstructions were calculated with a 50-year window (Fig. 4**c**). The finding highlights that the connection between the RH of the SPR and ASM was characterized by an unstable and nonstationary process through time. The coherence between them became weakened (enhanced) during the 1870s–1910s and 1960s–2010s (1800s–1860s and 1920s–1960s), when ENSO variance was high (low) (Fig. 4**d**).

Spatial correlations of the reconstructions with gridded global SSTs and 850hpa GPHs in the SPR and ASM were calculated for the three intervals 1871–1919, 1920–1960, and 1961–2015 (Fig. 5; **Fig. S8**). During the SPR (ASM) season, significant positive (negative) correlations with SSTs were found over the eastern equatorial tropical Pacific during the periods 1871–1919 and 1961–2015 (Fig. 5**a, 5c, 5d, 5f**). This ENSO (La Niña) related SST anomalies coheres with anomalous positive low-troposphere pressure variations around the western North Pacific (WNP) (the Japan Sea) (**Figs. S8a, S8c, S8d, S8f**), indicative of the seasonal movement of WPSH. The connection between the two reconstructions and SSTs during the 1920–1960 period is weak (Fig. 5**b, 5e**). Nevertheless, this period witnessed a band of significant negative pressure variations along the tropical zone (**Figs. S8b, S8e**), indicative of the Intertropical Convergence Zone (ITCZ).

4. Discussion

4.1. Wet and dry periods

Long-term variations of the two reconstructions derived from tree-ring earlywood and latewood $\delta^{18}O$ reveals a notable phase shift of hydroclimate during both the SPR and ASM over SEC in the 1920s (Fig. 4**a, 4b**). The hydroclimate variations of both seasons were generally low and fluctuated moderately prior to that. The 1920s–1960s period experienced the most pronounced and long-lasting wet conditions over the past two centuries. This wet interval was also expressed in an April–September precipitation reconstruction nearby based on *Fokienia hodginsii* tree-ring $\delta^{18}O$ (Xu et al., 2013) and other recorded evidence of flooding from local historical documentary data and stalagmite data (Zeng, 1992; Jiang et al., 2012). After a megadrought in the 1920 s (Liang et al., 2006; Fang et al., 2017), hydroclimate in northern China maintained remarkably wet conditions until the 1960s compared to the past four centuries (Li et al., 2009). Similarly, anomalously wet

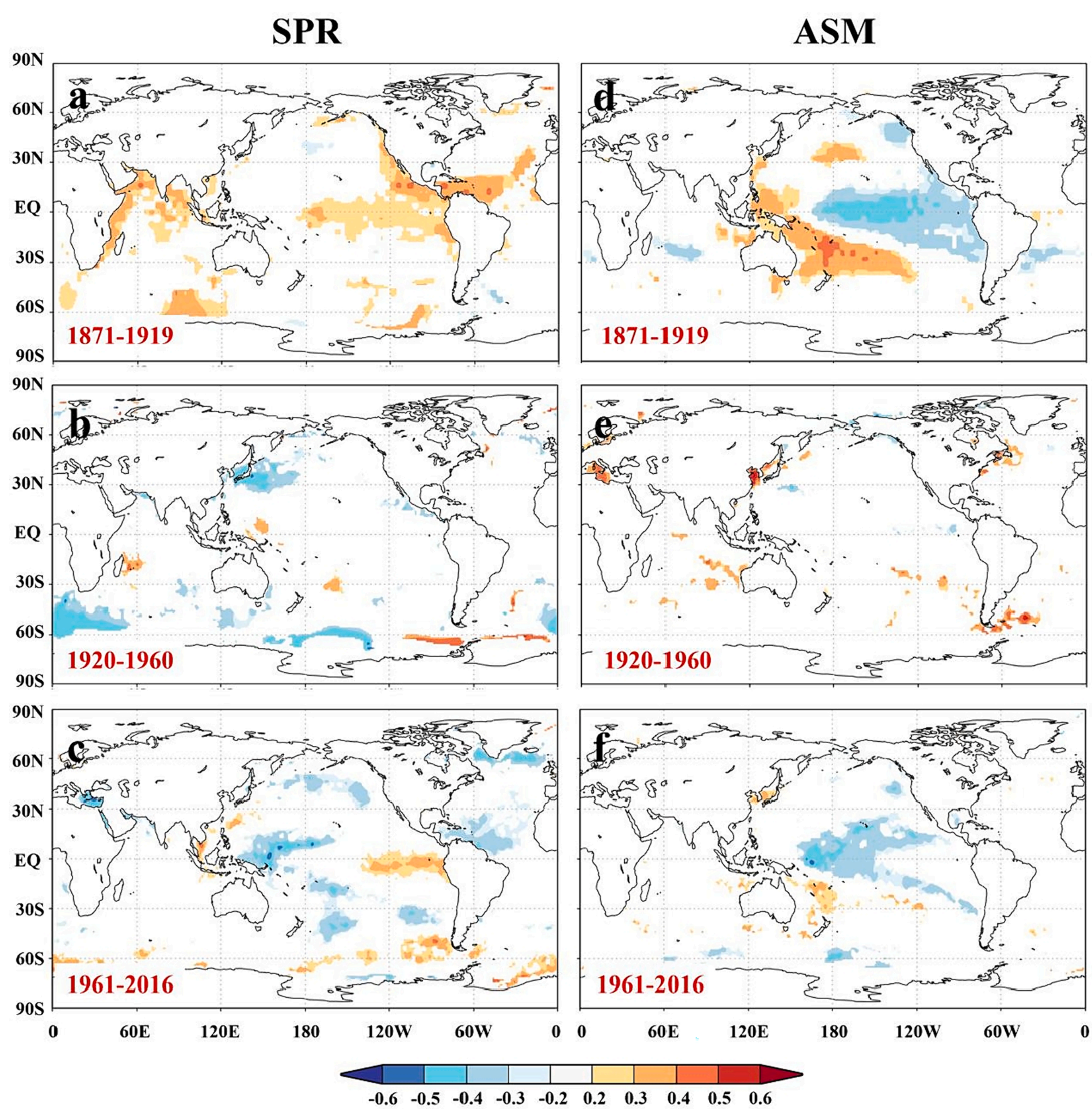

Fig. 5. Spatial correlations of the reconstructed hydroclimate variance with contemporaneous global SSTs for the periods 1871–1919 (a, d), 1920–1960 (b, e), and 1961–2015 (c, f) during SPR (a-c) and ASM (d-f), respectively. Correlations not significant at the 95% level have been masked out.

conditions are also observed in the middle-lower Yangtze River Basin during the 1920s-1960s (Xu et al., 2016, 2018; Wang et al., 2011). The monopole mode of hydroclimatic changes over East China coheres with an increase in thermal gradient between the Northern Hemisphere (NH) temperature and tropical ocean SSTs (**Fig. S9**), which coincides with a significant intensification of water vapor convergence from tropical oceans to East China (Li et al., 2009; Shi et al., 2019).

Analysis of instrumental data reveals a slight increase in rainfall variations of the SPR and ASM since the late 20th century in SEC (**Fig. S4**). However, an exceptional and sustained wetting trend occurred during the SPR over the 1970s–1990s, which may be related to weakened evaporation due to a dramatic decrease in spring temperature over SEC (Duan et al., 2011; Cai et al., 2018). Association of the southward movement of the cold center in China (Ma et al., 2012) is presumed to be teleconnected with a decrease in Arctic sea-ice area from a warming climate, which has changed the atmospheric circulations in the NH and caused broader meridional meanders at the mid-latitudes (Liu et al., 2012; Duan et al., 2013). Considering an expected increase of cold waves over SEC in the context of global warming (Ma et al., 2012; Duan et al., 2013), fluctuations of the SPR can be perhaps be expected to enhance in the future. Conversely, only a slight decline tendency was observed in effective rainfall changes during the ASM since the 1970s, due to an offset between increased rainfall and temperature.

4.2. ENSO weakens the co-variability between SPR and ASM

Our study revealed linkages between the hydroclimate of the SPR and ASM and the two leading tropical systems: the ITCZ and ENSO (Fig. 6). ENSO operates in the tropical Pacific Ocean and can modulate climate in remote extratropical areas via various teleconnections (Kumar et al., 1999; Li et al., 2013). However, the teleconnections become weakened when variance of ENSO was low (Webster & Yang, 1992; Xu et al., 2013; Zhou et al., 2020), and other atmosphere–ocean patterns may take the place of ENSO as the main driving factors for climate dynamics. Herein, when the ENSO variability was weakened, the ITCZ dominates the SPR and ASM co-variability.

The seasonal movement of ITCZ is modulated by the migration of the Sun's overhead position. When ITCZ is positioned near to the Equator during the SPR, the rising hot air from ITCZ moves poleward and descends over WNP through the Hadley Circulation, suggestive of a strong WPSH (Fig. 6**a**). This synoptic pattern is in favor of anomalous southwestlies over SEC, driving the SPR (Wu & Mao, 2016). During the ASM season, the location of ITCZ moves northward to the subtropics and its band becomes wider (Waliser & Gautier, 1993), causing the development of WPSH stretching from the Japan Sea to the coastal areas of Northeast China (Fig. 6**b**). The circulation pattern coheres with an increase in the strength of ASM, bringing water vapor into SEC (Liu & Li, 2011). Therefore, the hydroclimate in SPR and ASM reveals a good coherency without the disturbances of ENSO.

When ENSO variance is strong, both ENSO and ITCZ dominate the SPR and ASM co-variability. Unlike ITCZ with seasonal migration across latitudes, ENSO is coupled oceanic and atmospheric processes that are generally locked to the tropical Pacific Ocean. The atmospheric component of ENSO is the Walker Circulation, a west–east circulation system coupled with the SST anomalies (Wang et al., 1999; Wang & Weisberg, 2000). The anomalously sinking motion of the Walker Circulation during the warm phase of the ENSO occurs over western Pacific Ocean and induces a distinct anticyclone in the low troposphere, which is the key system that teleconnects East Asian hydroclimate and ENSO (Wang et al., 2000; Wu & Mao, 2016). In the SPR, the descending air from ITCZ also arrives at WNP at the same time, leading to a progressive enhancement of WPSH and westerly humidity convection into SEC (Fig. 6**c**). However, due to the northward migration of ITCZ during the ASM season, the ENSO-related downward motion leads to a reduction in northerly movement of the rising motion along ITCZ, and a relative weak WPSH around the south of the Japan Sea and the coastal area of northern China (Fig. 6**d**). This mode is similar to the Pacific–Japan/East Asia–Pacific (PJ/EAP) pattern of teleconnection (Nitta, 1987; Huang & Sun, 1992; Qian & Zhou, 2014), which leads to the weakening of the ASM. In addition, ENSO strongly favors WNP tropical cyclone activities that also impact hydroclimate of SEC dramatically in ASM season (Chan, 2000; Wu et al., 2004; Patricola et al., 2018). During episodes with high ENSO variance, it appears that the hydroclimate of SPR and ASM in SEC are modulated by different circulation patterns, and the co-variability between them tends to decrease.

5. Conclusion

Earlywood and latewood $\delta^{18}O$ records from *Pinus massoniana* trees in SEC were found to be sensitive to hydroclimatic changes during the SPR and ASM seasons, respectively, and were used to reconstruct long-term SPR and ASM changes from 1801 to 2015. The two reconstructions revealed a long-lasting pluvial conditions from the 1920s to the 1960s, which were associated with a particularly large land–ocean thermal

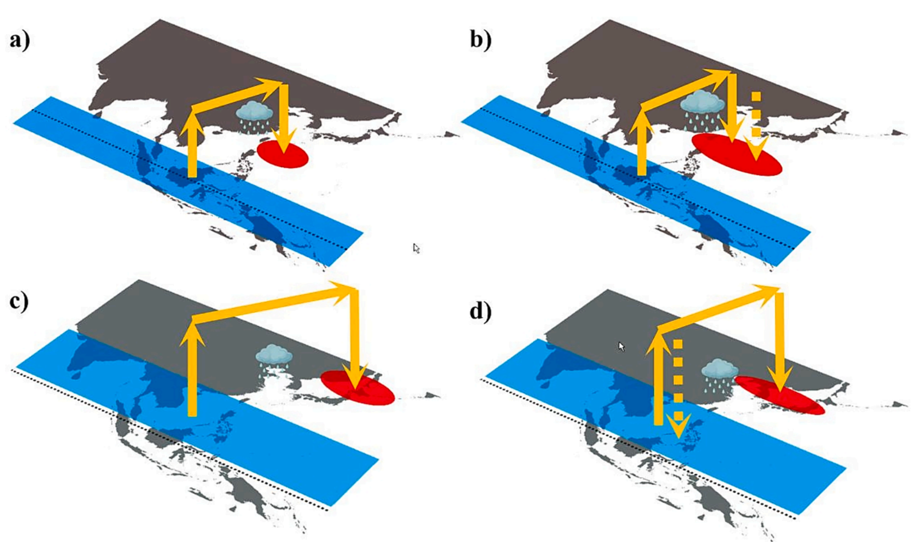

Fig. 6. Schematic diagram of the impact of circulation patterns on the hydroclimate conditions over SEC when the ENSO variance is low (a, b) and high (c, d) during SPR (a, c) and ASM (b, d) seasons, respectively. The red ellipse and blue band denote the anticyclone and ITCZ. (For interpretation of the references to colour in this figure legend, the reader is referred to the web version of this article.)

contrast. When the ENSO variance is low, both of the SPR and ASM are modulated by the co-varying ITCZ in both of the SPR and ASM seasons, causing in-phase SPR-ASM co-variability. When ENSO variance is high, the SPR and ASM co-variability is influenced by both the ENSO and ITCZ. This results in a weakening of the SPR–ASM co-variability as ENSO can offset the influence of ITCZ on rainfall changes in SEC.

CRediT authorship contribution statement

Feifei Zhou: Writing – original draft. **Keyan Fang:** Conceptualization, Supervision. **Fredrik Charpentier Ljungqvist:** Writing – review & editing. **Tinghai Ou:** Methodology, Software. **Jun Cheng:** Methodology. **Fen Zhang:** Writing – review & editing. **Zhengtang Guo:** Supervision.

Declaration of competing interest

The authors declare that they have no known competing financial interests or personal relationships that could have appeared to influence the work reported in this paper.

Data availability

Data will be made available on request.

Acknowledgement

We acknowledge supports from the National Science Foundation of China (42101082 and 42301058), the Natural Science Foundation of Fujian Province (2023J01496) the Strategic Priority Research Program of the Chinese Academy of Sciences (XDB26020000), fellowship for Youth Talent Support Program of Fujian Province and the innovation team project (IRTL1705) and the FORMAS (project 2017-01408). F.C.L. was supported by the Swedish Research Council (Vetenskapsrådet, grant no. 2018-01272), and conducted the work with this article as a Pro Futura Scientia XIII Fellow funded by the Swedish Collegium for Advanced Study through Riksbankens Jubileumsfond.

Appendix A. Supplementary data

Supplementary data to this article can be found online at https://doi.org/10.1016/j.jhydrol.2024.131080.

References

Amengual, A., Homar, V., Romero, R., Brooks, H., Ramis, C., Gordaliza, M., Alonson, S., 2014. Projections of heat waves with high impact on human health in Europe. Global Planet. Change 119, 71–84.

Bose, T., Sengupta, S., Chakraborty, S., Borgaonkar, H., 2016. Reconstruction of soil water oxygen isotope values from tree ring cellulose and its implications for paleoclimate studies. Quat. Int. 425, 387–398.

Cai, Q., Liu, Y., Duan, B., Sun, C., 2018. Regional difference of the start time of the recent warming in eastern China: prompted by a 165-year temperature record deduced from tree rings in the Dabie Mountains. Clim. Dynam. 50, 2157–2168.

Chan, J.C., 2000. Tropical cyclone activity over the western North Pacific associated with El Niño and La Niña events. J. Clim. 13, 2960–2972.

Compo, G.P., Whitaker, J.S., Sardeshmukh, P.D., Matsui, N., Allan, R.J., Yin, X., Gleason, B.E., Vose, R.S., Rutledge, G., Bessemoulin, P., Brönnimann, S., Brunet, M., Crouthamel, R.I., Grant, A.N., Groisman, P.Y., Jones, P.D., Kruk, M.C., Kruger, A.C., Marshall, G.J., Maugeri, M., Mok, H.Y., Nordli, Ø., Ross, T.F., Trigo, R.M., Wang, X. L., Woodruff, S.D., Worley, S.J., 2011. The Twentieth Century Reanalysis Project. Q J Roy Meteor Soc. 137, 1–28.

Dannenberg, M.P., Wise, E.K., 2016. Seasonal climate signals from multiple tree ring metrics: a case study of *Pinus ponderosa* in the upper Columbia River Basin. J. Geophys. Res. Biogeo. 121, 1178–1189.

Duan, J., Zhang, Q.B., Lv, L., Zhang, C., 2011. Regional-scale winter–spring temperature variability and chilling damage dynamics over the past two centuries in southeastern China. Clim Dynam. 39, 919–928.

Duan, J., Zhang, Q., Lv, L., 2013. Increased variability in cold-season temperature since the 1930s in subtropical china. J. Clim. 26, 4749–4757.

Fang, K., Frank, D., Zhao, Y., Zhou, F., Seppä, H., 2015. Moisture stress of a hydrological year on tree growth in the Tibetan Plateau and surroundings. Environ. Res. Lett. 10, 034010.

Fang, K., Guo, Z., Chen, D., Linderholm, H.W., Li, J., Zhou, F., Guo, G., Dong, Z., Li, Y., 2017. Drought variation of western Chinese Loess Plateau since 1568 and its linkages with droughts in western North America. Clim. Dynam. 49, 3839–3850.

Fritts, H.C., 1976. Tree rings and climate. Academic Press, London.

Green, J.W., 1963. Wood cellulose. In: Whistler, R.L. (Ed.), Methods in Carbohydrate Chemistry. Academic Press, New York, pp. 9–12.

Griffin, D., Meko, D.M., Touchan, R., Leavitt, S.W., Woodhouse, C.A., 2011. Latewood chronology development for summer-moisture reconstruction in the US southwest. Tree-Ring Res. 67, 87–101.

Huang, J., Liu, G., Zhao, X., 2004. The influence of subtropical high indexes and polar vortex indexes on the summertime precipitation in China. Acta Meteorol Sin. 65, 131–137.

Huang, R., Sun, F., 1992. Impacts of the tropical western Pacific on the East Asian summer monsoon. J. Meteorol. Soc. Jpn 70, 243–256.

Jiang, X., Li, Z., Li, J., Kong, X., Guo, Y., 2012. Stalagmite $\delta^{18}O$ record from Yuhua Cave over the past 500 years and its regional climate significance. Sci. Geogr. Sin. 32, 207–212.

Kumar, K.K., Rajagopalan, B., Cane, M.A., 1999. On the weakening relationship between the Indian monsoon and ENSO. Science 284, 2156–2159.

Leavitt, S.W., 2010. Tree-ring C-H-O isotope variability and sampling. Sci. Total Environ. 408, 5244–5253.

Li, J., Cook, E.R., Chen, F., Davi, N., D'Arrigo, R., Gou, X., Wright, W.E., Fang, K., Jin, L., Shi, J., Yang, T., 2009. Summer monsoon moisture variability over China and Mongolia during the past four centuries. Geophys. Res. Lett. 36, L22705.

Li, J., Xie, S.P., Cook, E.R., Morales, M.S., 2013. El Niño modulations over the past seven centuries. Nat. Clim. Chang. 3, 822–826.

Liang, E., Liu, X., Yuan, Y., Qin, N., Fang, X., Lei, H., Zhu, H., Wang, L., Shao, X., 2006. The 1920s drought recorded by tree rings and historical documents in the semi-arid and arid areas of northern China. Clim. Change 79, 403–432.

Liu, J., Curry, J.A., Wang, H., Song, M., Horton, R.M., 2012. Impact of declining Arctic sea ice on winter snowfall. P Natl Acad Sci USA 109, 4074–4079.

Liu, Y., Kim, M.C., Song, H., Li, Q., Li, C., Nakatsuka, T., An, Z., Zhou, W., Cai, Q., Li, J., Steven, W.L., Sun, C., Mei, R., Shen, C., Chan, M., Sun, J., Yan, L., Lei, Y., Ma, Y., Li, X., Chen, D., Linderholm, H.W., 2017. Recent enhancement of central Pacific El Niño variability relative to last eight centuries. Nat. Commun. 8, 15386.

Liu, N., Li, Z., 2011. Relationship of the western Pacific warm pool SST anomaly and summer precipitation in China. Meteorology & Disaster Reduction Research. 34, 8–13.

Liu, X., Shao, X., Liang, E., Chen, T., Qin, D., An, W., Xu, G., Sun, W., Wang, Y., 2009. Climatic significance of tree-ring $\delta^{18}O$ in the Qilian Mountains, northwestern China and its relationship to atmospheric circulation patterns. Chem. Geol. 268, 147–154.

Ljungqvist, F.C., Piermattei, A., Seim, A., Krusic, P.J., Büntgen, U., He, M., Kirdyanov, A. V., Luterbacher, J., Schneider, L., Seftigen, K., Stahle, D.W., Villalba, R., Yang, B., Esper, J., 2020. Ranking of tree-ring based hydroclimate reconstructions of the past millennium. Quaternary Sci Rev. 230, 106074.

Loader, N., Robertson, I., Barker, A., Switsur, V., Waterhouse, J., 1997. An improved technique for the batch processing of small wholewood samples to α-cellulose. Chem. Geol. 136, 313–317.

Ma, T., Wu, Z., Jiang, Z., 2012. How does coldwave frequency in China respond to a warming climate? Clim Dynam. 39, 2487–2496.

Managave, S., Shimla, P., Yadav, R.R., Ramesh, R., Balakrishnan, S., 2020. Contrasting centennial-scale climate variability in high mountain Asia revealed by a tree-ring oxygen isotope record from Lahaul-Spiti. Geophys. Res. Lett. 47 e2019GL086170.

Mao, J., Chan, J., Wu, G., 2014. Relationship between the onset of the South China Sea summer monsoon and the structure of the Asian subtropical anticyclone. J. Meteorol. Soc. Jpn 82, 845–859.

Mccarroll, D., Loader, N., 2004. Stable isotopes in tree rings. Quaternary Sci Re. 23, 771–801.

Meko, D., Graybill, D.A., 1995. Tree-ring reconstruction of upper Gila River discharge. J Am Water Resour As 31, 605–616.

Nitta, T., 1987. Convective activities in the tropical western Pacific and their impact on the Northern Hemisphere summer circulation. J. Meteorol. Soc. Jpn. Ser. II. 65, 373–390.

Patricola, C.M., Camargo, S.J., Klotzbach, P.J., Saravanan, R., Chang, P., 2018. The influence of ENSO flavors on western North Pacific tropical cyclone activity. J. Clim. 31, 5395–5416.

Peng, J., Chen, L., Zhang, Q., 2005. Multi-scale variations of snow cover over QXP and tropical Pacific SST and their influences on summer rainfall in China. Plateau Meteorol. 24, 366–377.

Piao, S., Ciais, P., Huang, Y., Shen, Z., Peng, S., Li, J., Zhou, L., Liu, H., Ma, Y., Ding, Y., Friedlingstein, P., Liu, C., Tan, K., Yu, Y., Zhang, T., Fang, J., 2010. The impacts of climate change on water resources and agriculture in China. Nature 467, 43–51.

Qian, C., Zhou, T., 2014. Multidecadal variability of North China aridity and its relationship to PDO during 1900–2010. J. Clim. 27, 1210–1222.

Rayner, N., Parker, D.E., Horton, E.B., Folland, C.K., Alexander, L.V., Rowell, D.P., Kent, E.C., Kaplan, A., 2003. Global analyses of sea surface temperature, sea ice, and night marine air temperature since the late nineteenth century. J. Geophys. Res. Atmos. 108, D14.

Seftigen, K., Fuentes, M., Ljungqvist, F.C., Björklund, J., 2020. Using Blue Intensity from drought-sensitive *Pinus sylvestris* in Fennoscandia to improve reconstruction of past hydroclimate variability. Clim Dynam. 55, 579–594.

Shi, F., Goosse, H., Klein, F., Zhao, S., Liu, T., Guo, Z., 2019. Monopole mode of precipitation in East Asia modulated by the South China Sea over the last four centuries. Geophys. Res. Lett. 46.
Slivinski Coauthors, L.C., 2019. Towards a more reliable historical reanalysis: Improvements for version 3 of the Twentieth Century Reanalysis system. Q J Roy Meteor Soc. 145, 2876–2908.
Tabari, H., Willems, P., 2018. Seasonally varying footprint of climate change on precipitation in the Middle East. Sci. Rep. 8, 4435.
Tao, S., Chen, L., 1987. A review of recent research on the East Asian summer monsoon in China. In: Chang, C., Krishnamurti, T. (Eds.), Monsoon meteorology. Oxford University Press, London, pp. 60–92.
Tian, S., Yasunari, T., 1998. Climatological aspects and mechanism of spring persistent rains over central China. J. Meteorol. Soc. Jpn 76, 57–71.
Trenberth, K.E., Stepaniak, D.P., 2001. Indices of El Niño evolution. J. Clim. 14, 1697–1701.
Trouet, V., Van Oldenborgh, G.J., 2013. KNMI Climate Explorer: A web-based research tool for high-resolution paleoclimatology. Tree-Ring Res. 69, 3–13.
Waliser, D.E., Gautier, C., 1993. A satellite-derived climatology of the ITCZ. J. Clim. 6, 2162–2174.
Wan, R., Wu, G., 2009. Temporal and spatial distributions of the spring persistent rains over Southeastern China. Acta Meteorol Sin. 23, 598–608.
Wan, R., Wang, T., Wu, G., 2008. Temporal variations of the spring persistent rains and SCS subtropical high and their correlations to the circulation and precipitation of the East Asian summer monsoon. Acta Meteorol Sin. 66, 800–807.
Wang, L., Fang, K., Chen, D., Dong, Z., Zhou, F., Li, Y., Zhang, P., Ou, T., Guo, G., Cao, X., Yu, M., 2018. Intensifified variability of the El Niño–Southern Oscillation enhances its modulations on tree growths in southeastern China over the past 218 years. Int. J. Climatol. 38, 5293–5304.
Wang, C., Weisberg, R.H., Virmani, J.I., 1999. Western Pacific interannual variability associated with the El Niño–Southern Oscillation. J. Geophys. Res. Oceans 104, 5131–5149.
Wang, C., Weisberg, R.H., 2000. The 1997–98 El Niño evolution relative to previous El Niño events. J. Clim. 13, 488–501.
Wang, B., Wu, R., Fu, X., 2000. Pacific-East Asian teleconnection: how does ENSO affect East Asian climate? J. Clim. 13, 1517–1536.
Wang, M., Zheng, H., Xie, X., Fan, D., Yang, S., Zhao, Q., Wang, K., 2011. A 600-year flood history in the Yangtze River drainage: comparison between a subaqueous delta and historical records. Chinese Sci Bull. 056, 188–195.
Webster, P.J., Yang, S., 1992. Monsoon and ENSO: Selectively interactive systems. Q J Roy Meteor Soc. 118, 877–926.
Wilson, R.J.S., Cook, E.R., D'Arrigo, R.D., Riedwyl, N., Evans, M.N., Tudhope, A.W., Allan, R.J., 2010. Reconstructing ENSO: the influence of method, proxy data, climate forcing and teleconnections. J Quaternary Sci. 25, 62–78.
Wu, M., Chang, W., Leung, W., 2004. Impacts of El Niño–Southern Oscillation events on tropical cyclone landfalling activity in the western North Pacific. J. Clim. 17, 1419–1428.
Wu, X., Mao, J., 2016. Interdecadal modulation of ENSO-related spring rainfall over South China by the Pacific Decadal Oscillation. Clim Dynam. 47, 3203–3220.
Xu, C., Zheng, H., Nakatsuka, T., Sano, M., 2013. Oxygen isotope signatures preserved in tree ring cellulose as a proxy for April–September precipitation in Fujian, the subtropical region of southeast China. J. Geophys. Res. Atmos. 118, 12, 805–812, 815.
Xu, C., Ge, J., Nakatsuka, T., Yi, L., Zheng, H., Sano, M., 2016. Potential utility of tree ring $\delta^{18}O$ series for reconstructing precipitation records from the lower reaches of the Yangtze River, southeast China. J. Geophys. Res. Atmos. 121, 3954–3968.
Xu, C., Shi, J., Zhao, Y., Nakatsuka, T., Sano, M., Shi, S., Guo, Z., 2018. Early summer precipitation in the lower Yangtze River basin for AD 1845–2011 based on tree-ring cellulose oxygen isotopes. Clim Dynam. 52, 1583–1594.
Yang, F., Lau, K., 2004. Trend and variability of China precipitation in spring and summer: linkage to sea-surface temperatures. Int. J. Climatol. 24, 1625–1644.
Zeng, C., 1992. Flood damages in history and problems on future flood protection in the lower reaches of the Minjiang River. Trop. Geogr. 12, 45–52.
Zhou, F., Fang, K., Zhang, F., Dong, Z., 2020. Hydroclimate change encoded in tree rings of fengshui woods in southeastern China and its teleconnection with El Niño–Southern Oscillation. Water Res Res. 56 e2018WR024612.